Virologica Sinica 39 (2024) 619–631

Contents lists available at ScienceDirect

Virologica Sinica

journal homepage: www.keaipublishing.com/en/journals/virologica-sinica
www.virosin.org

Research Article

Structural and functional insights into the 2′-O-methyltransferase of SARS-CoV-2

Jikai Deng [a,1], Feiyu Gong [a,1], Yingjian Li [a], Xue Tan [a], Xuemei Liu [a], Shimin Yang [a], Xianying Chen [a], Hongyun Wang [a], Qianyun Liu [a], Chao Shen [a], Li Zhou [a,b], Yu Chen [a,b,*]

[a] State Key Laboratory of Virology, RNA Institute, College of Life Sciences and Frontier Science Center for Immunology and Metabolism, Wuhan University, Wuhan, 430072, China
[b] Animal Bio-Safety Level III Laboratory/Institute for Vaccine Research, Wuhan University School of Medicine, Wuhan, 430071, China

ARTICLE INFO

Keywords:
SARS-CoV-2
nsp16/nsp10
2′-O-Methyltransferase
3-Dimensional structure
Molecular mechanism
Inhibitors

ABSTRACT

A unique feature of coronaviruses is their utilization of self-encoded nonstructural protein 16 (nsp16), 2′-O-methyltransferase (2′-O-MTase), to cap their RNAs through ribose 2′-O-methylation modification. This process is crucial for maintaining viral genome stability, facilitating efficient translation, and enabling immune escape. Despite considerable advances in the ultrastructure of SARS-CoV-2 nsp16/nsp10, insights into its molecular mechanism have so far been limited. In this study, we systematically characterized the 2′-O-MTase activity of nsp16 in SARS-CoV-2, focusing on its dependence on nsp10 stimulation. We observed cross-reactivity between nsp16 and nsp10 in various coronaviruses due to a conserved interaction interface. However, a single residue substitution (K58T) in SARS-CoV-2 nsp10 restricted the functional activation of MERS-CoV nsp16. Furthermore, the cofactor nsp10 effectively enhanced the binding of nsp16 to the substrate RNA and the methyl donor S-adenosyl-L-methionine (SAM). Mechanistically, His-80, Lys-93, and Gly-94 of nsp10 interacted with Asp-102, Ser-105, and Asp-106 of nsp16, respectively, thereby effectively stabilizing the SAM binding pocket. Lys-43 of nsp10 interacted with Lys-38 and Gly-39 of nsp16 to dynamically regulate the RNA binding pocket and facilitate precise binding of RNA to the nsp16/nsp10 complex. By assessing the conformational epitopes of nsp16/nsp10 complex, we further determined the critical residues involved in 2′-O-MTase activity. Additionally, we utilized an *in vitro* biochemical platform to screen potential inhibitors targeting 2′-O-MTase activity. Overall, our results significantly enhance the understanding of viral 2′-O methylation process and mechanism, providing valuable targets for antiviral drug development.

1. Introduction

Eukaryotic cells possess a unique defense mechanism that specifically recognizes the 5′-terminal exposed mRNA molecules, triggering an innate immune response through a cascade of signal transduction events to eliminate the exposed triphosphate mRNA (Liu and Kiledjian, 2006; Nallagatla et al., 2008). The invasion of RNA viruses into the host is accompanied by extensive replication and propagation of viral RNA molecules. Therefore, under selective pressure, viruses have evolved mechanisms to hide the 5′-terminal triphosphates of RNA, thereby avoiding recognition by the innate immune system (Chen and Guo, 2016; Hornung et al., 2006). One strategy involves emulating endogenous mRNA molecules by capping the 5′ end of the viral genome or subgenome (Hornung et al., 2006). The majority of coronaviruses follow a traditional mode of capping: (i) The phosphate bonds within β-phosphate and γ-phosphate of the exposed triphosphate RNA are cleaved by RNA triphosphatase (RTPase), generating a 5′-diphosphate end (5′-ppN, N, A or G) (Ivanov and Ziebuhr, 2004; Yan et al., 2021a). (ii) Guanine nucleoside is subsequently conjugated with 5′-diphosphate RNA to generate the crucial structure (GpppN) upon the action of guaninetransferase (GTase) (Yan et al., 2021a). (iii) GpppN is methylated at the N7-position upon the action of N7-methyltransferase (N7-MTase) to produce cap-0 structures (^{7Me}GpppN) (Chen et al., 2009). (iv) ^{7Me}GpppN is further methylated at the ribose 2′-O-position of the first nucleotide by 2′-O-methyltransferase (2′-O-MTase) to create cap-1 structures (^{7Me}GpppN$_m$) (Decroly et al., 2008a). Upon cell entry, coronaviral genomic RNA is translated to

* Corresponding author.
E-mail address: chenyu@whu.edu.cn (Y. Chen).
[1] Jikai Deng and Feiyu Gong contributed equally to this work.

https://doi.org/10.1016/j.virs.2024.07.001
Received 24 November 2023; Accepted 2 July 2024
Available online 3 July 2024

generate non-structural protein (nsp) from two open reading frames (ORFs), ORF1a and ORF1b (Chen et al., 2020). These non-structural proteins are assembled into the replication transcription complex (RTC) and play key roles in the replication of genome-length viral RNAs and in the transcription of viral mRNAs (Ziebuhr, 2005; Chen et al., 2022). Among them, non-structural protein 16 (nsp16) exhibits 2′-O-MTase activity by converting the cap-0 structure into the cap-1 structure (Chen et al., 2011; Zeng et al., 2016; Decroly et al., 2008a). The cap structure is essential for enhancing viral replication (Smith et al., 2015), stabilizing viral RNA translation (Ray et al., 2006), evading host innate immune recognition (Zust et al., 2011), and resisting IFN-mediated antiviral responses (Rehwinkel et al., 2010; Deng et al., 2024).

In recent years, the structures of SARS-CoV-2 RTC and capping synthetic intermediates have been reported (Park et al., 2022; Yan et al., 2021a, 2021b). These findings accelerate our understanding of the capping process. In this study, we focused on characterizing the biochemical properties of the SARS-CoV-2 2′-O-MTase. Our findings revealed that the cofactor nsp10 played a crucial role in regulating the binding process of nsp16 to the substrate RNA and the methyl donor SAM. We further identified the critical residues associated with 2′-O-MTase activity, and demonstrated the unique mechanism underlying the binding of nsp16/nsp10 complex to SAM and RNA. Additionally, we conducted compound screening to target 2′-O-MTase activity. These results expand our comprehension of the capping mechanism, thereby fostering the development of broad-spectrum anti-coronavirus drugs.

2. Material and methods

2.1. Radioactive reagents

S-Adenosyl (methyl-^{3}H) methionine (67.3 Ci/mmol) and (α-^{32}P) GTP (3000 Ci/mmol) were obtained from PerkinElmer.

2.2. Cloning, optimization, and mutation

The coding sequences of nsp16 (NCBI reference sequence: YP_009725311) and nsp10 (NCBI reference sequence: YP_009742617) were optimized using the GenScript Optimum Gene™ algorithm. The optimized codons were cloned into pET30a vector downstream of a His-tag sequence. The mutants were numbered from the beginning of the nsp16 sequence: Y30A, K38A, G39A, N43A, K46A, Y47A, G71A, A72F, G73A, S74A, P80A, G81A, D99A, L100A, N101A, D102A, S105A, D106A, D114A, C115A, D130A, M131A, Y132A, K137A, F149A, K170A, T172A, E173A, H174A, N198A, S201A, or the nsp10 sequence: K43A, L45A, K58T, H80A, K93A, G94A, Y96A, Y96F. All plasmids were identified via DNA sequencing.

2.3. Expression and purification of protein

E. coli BL21 (DE3) was transformed with a corresponding plasmid, and then was grown in Luria broth (LB) supplemented with kanamycin at 37 °C. Upon reaching an optical density at 600 nm (OD600) of 0.6, isopropyl β-D-1-thiogalactopyranoside (IPTG) was added to a final concentration of 0.4 mM. After incubation at 16 °C for 16 h, ultrasonic centrifugation was conducted by an ultrasonic cell disruptor. The cleared lysates were incubated with nickel-nitrilotriacetic acid (Ni-NTA) resin for 1 h. Proteins were eluted with 40 mM Tris–HCl supplemented with 250 mM imidazole. The nsp10 and nsp16 were further purified using an Enrich SEC 650 Column (BIO-RAD). Protein purity was assessed by SDS-PAGE and visualized with Coomassie blue staining. SARS-CoV-2 nsp10 (pp1a residues 4265 to 4384; 120 amino acids) fused with an N-terminal His-tag which was confirmed by SDS-PAGE to be about 15 kDa. SARS-CoV-2 nsp16 (pp1ab residues 6800 to 7095; 296 amino acids) carrying an N-terminal His-tag was approximately 33 kDa. The nsp10 and nsp16 of SARS-CoV, MERS-CoV, and MHV were expressed and purified using the methodology previously described (Chen et al., 2011).

2.4. Preparation of multiple RNA substrates

RNA substrate, ^{7Me}GpppAC$_{20}$, was transcribed *in vitro*. To initiate transcription, we added a bacteriophage T7 promoter (TAATACGACTCACTATA) to the primers. A HiScribe™ T7 kit (New England BioLabs) was used to configure a 20 μL reaction system with 2 μg of dsDNA as a template according to the manufacturer's instructions. After *in vitro* transcription, the dsDNA template was digested by adding 2 units of DNase I and incubating at 37 °C for 15 min. The RNA transcribed *in vitro* was further extracted with phenol-chloroform, precipitated with 100% alcohol containing sodium acetate, rinsed with 75% alcohol, and suspended in RNase-free water. Nanodrop 2000c (Thermo Scientific) was used for RNA quantification. Instead of SAM, 10 mCi of S-adenosyl (methyl^{-3}H) methionine was used as the methyl donor to produce the ^{3}H-labeled cap structures (*^{7Me}GpppAC$_{20}$). The ^{32}P-labeled RNA substrates (G*pppA, ^{7Me}G*pppA and ^{7Me}G*pppA$_{m}$; the asterisks indicate that the following phosphates were α-GTP-^{32}P-labeled) used for thin-layer chromatography (TLC) were synthesized as described previously (Chen et al., 2009; Deng et al., 2024).

2.5. Biochemical assays for MTase activity

For TLC, an 8.5 μL reaction mixture was prepared with 40 mM Tris-HCl (pH 7.0), 2 mM $MgCl_2$, 2 mM DTT, 10 units RNase inhibitor, 0.2 mM SAM. Subsequently, 1 μg of purified proteins and 2000 cpm of ^{32}P-labeled RNA substrates were added. The mixture was incubated at 30 °C for 2 h. To release the cap structures, 0.5 μL of nuclease P1 (New England BioLabs, 100 unit/μL) and 1 μL of RNase-free water were added at 50 °C for 30 min. The samples were then applied to polyethyleneimine cellulose-F plates (Merck) and developed in a mobile phase of 0.4 M ammonium sulfate. A PhosphorImager was utilized to scan the chromatogram for the detection and analysis of the range of ^{32}P-labeled cap structures.

The assays of ^{3}H-methyl-incorporation MTase activity were performed in a 20 μL reaction system [containing 50 mM Tris–HCl (pH 7.0), 2 mM $ZnCl_2$, 2 mM DTT, 0.01 mM SAM, 0.3 μCi of S-adenosyl (methyl-^{3}H) methionine, 40 units of RNase inhibitor, 1 μg of purified proteins and 3 μg of RNA substrates] at 30 °C for 1 h. The –CH_3 of S-adenosyl (methyl-^{3}H) methionine was transferred to the cap-0 structure to form a cap-1 structure through the 2′-O-MTase. The ^{3}H-labeled products were isolated by DEAE-Sephadex A-50 columns, as described previously (Ahola et al., 1997; Chen et al., 2011), liquid scintillation counter (PerkinElmer) was used for quantification. The cpm value was used to reflect 2′-O-MTase activity.

2.6. RNA binding assay

A total of 4 μg of purified His$_6$-proteins and 3 μg of ^{3}H-labeled RNA substrates were combined in 100 μL binding buffer (comprising 40 mM Tris–HCl, 2 mM $MgCl_2$) and rotation at 4 °C overnight. Afterward, 20 μL Ni-NTA affinity resin was gently added at 4 °C for 30 min to allow binding of the ^{3}H-labeled RNA-His$_6$ protein complexes. The supernatant was then removed, and the resin-protein-RNA complexes were washed twice with the same binding buffer. Finally, the complexes were resuspended in 100 μL of binding buffer. A 30 μL aliquot of this suspension was allocated for Western blot analysis, and the remaining volume was assessed for radioactivity using liquid scintillation counting (Chen et al., 2011).

2.7. Isothermal titration calorimetry

Freshly purified nsp16 and nsp10 proteins were mixed, and their final concentrations were 15 mM and 15 mM (1:1), respectively. Then nsp16,

nsp10, and nsp16/nsp10 complex were dialyzed against the same solution (5 mM Tris–HCl buffer with 5 mM $MgCl_2$, pH 7.0) overnight at 4 °C, extensively to remove glycerol and DTT. In addition, we subjected the co-expressed nsp16/nsp10 complex to denaturation/refolding treatment, as previously reported (Lin et al., 2020).

Subsequently, ITC experiments were conducted with 20 μM SARS-CoV-2 nsp16, nsp10 and nsp16/nsp10 complex and 200 μM $^{7Me}GpppAC_{20}$ via Malvern MICROCAL PEAQ-ITC machine. This experimental method produced single 0.4 μL injections, followed by another injection of 18.2 μL. Prior to data analysis, the corresponding concentration of $^{7Me}GpppAC_{20}$ solution was injected into 50 mM Tris–HCl alone, which was used as the control. Refined power-time curves reflecting thermodynamic alterations were subsequently generated and analyzed by employing data using MicroCal PEAQ-ITC Analysis software. The binding stoichiometry, N, the standard molar enthalpy changes for the binding, $\Delta_b H^0_m$, the dissociation constant, K_d, the standard molar free energy change, $\Delta_b G^0_m$, and the standard molar entropy change, $\Delta_b S^0_m$, were thus obtained. The identical approach was employed to monitor the thermodynamic alterations during SAM binding to the nsp16/nsp10 complex of SARS-CoV-2.

2.8. Multiple-sequence alignment and 3D structure modeling

Protein sequences of various coronaviruses were retrieved from the NCBI database. These sequences underwent multiple-sequence alignment, which was subsequently integrated with the Protein Data Bank (PDB) file using ESPript 3.x (Robert and Gouet, 2014). Structural details of the SARS-CoV-2 nsp16/nsp10 complex (Protein Data Bank accession number 6WKS) were elucidated using the PDB bank. PyMOL software was employed for further assessing the structural characteristics. The ZDOCK server was utilized for predicting the interaction of protein-protein complexes (Pierce et al., 2014).

2.9. Analysis of NGS RNA-seq data

The number of reads for nsp10 and nsp16 in Vero E6 infected with SARS-CoV-2 was quantified as previously described (Wang et al., 2021). We further used R 4.1.0 to draw a stacked bar chart.

3. Results

3.1. Nsp16 shows 2′-O-methyltransferase activity in the presence of cofactor nsp10

To investigate the molecular mechanism of SARS-CoV-2 nsp16/nsp10 as a 2′-O-MTase, we expressed and purified recombinant SARS-CoV-2 nsp16 and nsp10 (Supplementary Figs. S1A and B). We then selectively isolated and purified $^{7Me}GpppAC_{20}$ (cap-0 structure) as the reaction substrate, followed by incubation with the corresponding proteins. During the methylation process, the ^{3}H-labeled methyl group was transferred from SAM to the $^{7Me}GpppAC_{20}$ substrate, resulting in the formation of the $^{7Me}GpppA_mC_{20}$ (cap-1 structure). This product could be quantitatively utilized to assess 2′-O-MTase activity via liquid scintillation detection (Ahola et al., 1997). As is shown in Fig. 1A, only in the presence of nsp10 did nsp16 show significant 2′-O-MTase activity. We also synthesized a ^{7Me}G*pppA-RNA capping substrate (where the * indicates that the following phosphate was ^{32}P-labeled) for TLC analysis (Fig. 1B). The mixture of nsp16/nsp10 gave rise to the cap-1 structure, further confirming the requirement of nsp10 as a cofactor for the proper activity of nsp16. Furthermore, it has been demonstrated that nsp10 enhances the activity of nsp16 2′-O-MTase in a dose-dependent manner. For maximum stimulation of SARS-CoV nsp16, at least a 6-fold molar amount of nsp10 is required (Bouvet et al., 2010; Chen et al., 2011). However, in the case of SARS-CoV-2 nsp16, each molecule can function optimally with one molecule of nsp10 (Fig. 1C). To further explore the dynamic changes of nsp16/nsp10 ratio upon the physiological state of the viral infection, a global analysis was conducted in Vero E6 cells during the early stages of SARS-CoV-2 infection (Wang et al., 2021). We counted the number of leaders-body junctions for the sgRNAs based on the first annotated genes downstream of the junction or other group (Fig. 1D). The ratio of nsp16 sgRNA to nsp10 sgRNA at the junction sites was found to be approximately 1:1 in the NGS data. These results indicated that upon initiation of the capping reaction, each SARS-CoV-2 nsp16 molecule can form a complex with at least one nsp10 molecule, leading to maximum 2′-O-MTase activity.

To determine whether the stimulatory effect of nsp10 as a cofactor is irreplaceable, replacement testing was performed using nsp16 and nsp10 from SARS-CoV-2, MERS-CoV, SARS-CoV, and MHV, which belong to the β-coronaviruses (Fig. 1E and F). The results suggested that SARS-CoV-2 nsp16 could be stimulated to a similar level by its cognate nsp10. To further assess why nsp16 can recognize nsp10 from other coronaviruses, we performed a multiple-sequence alignment of nsp16 and nsp10 across various coronaviruses. It was observed that the critical residues at the nsp16/nsp10 interface were conserved among coronaviruses (Supplementary Figs. S2A and 2B). This suggested that the mechanism through which nsp10 stimulated nsp16 may be relatively conserved.

Notably, SARS-CoV-2 nsp10 showed limited activation of MERS-CoV nsp16 function, possibly attributed to disparities in their recognition motifs. The coordinates of the SARS-CoV-2 nsp16/nsp10 complex or MERS-CoV nsp16/nsp10 complex with and without SAM or $^{7Me}GpppA$ RNA have been extensively deposited in the Protein Data Bank (PDB) (Viswanathan et al., 2020; Krafcikova et al., 2020; Lin et al., 2020; Mahalapbutr et al., 2020; Rosas-Lemus et al., 2020; Wilamowski et al., 2021). To verify our hypothesis, we conducted a crystal structure comparison. Initially, we superimposed the structures of the MERS-CoV nsp16/nsp10 complex (PDB 5YN5) and the SARS-CoV-2 nsp16/nsp10 complex (PDB 6XKM). The comparison revealed a strong similarity (RMSD ~0.593 Å) between the nsp16 of SARS-CoV-2 and MERS-CoV, with subtle differences in the conformation of the loop regions 28–40 and 131–142. Additionally, we observed that the density of the N-terminal region 1–17 (Helix) of nsp10 was untraceable in SARS-CoV-2, while it was clearly observed in MERS-CoV (Supplementary Fig. S2C). These findings align with previous studies conducted by Rogstam A. et al. and Lin S. et al. (Lin et al., 2020; Rogstam et al., 2020). We further performed an analysis of the interacting interface between SARS-CoV-2 or MERS-CoV nsp16 and nsp10 (Fig. 1G and H). It was found that significant contacts at the nsp10 and nsp16 interface involved multiple residues. In SARS-CoV-2, the intermolecular hydrogen bonds exist between Lys-43 of nsp10 and Lys-38 of nsp16, Leu-45 of nsp10 and Gln-87 of nsp16, Lys-93 of nsp10 and Ser-105 of nsp16, Gln-94 of nsp10 and Asp-106 of nsp16, and Tyr-96 of nsp10 and Ala-83 of nsp16. Two salt bridges exist between His-80 of nsp10 and Asp-102 of nsp16. In MERS-CoV, additional intermolecular hydrogen bonds exist between Aln-40 of nsp10 and His-41 of nsp16, Lys-58 of nsp10 and Gln-87 of nsp16, which were not present in SARS-CoV-2. We utilized the ZDOCK server, an interactive docking prediction service for protein-protein complexes (Pierce et al., 2014), to perform molecular docking of MERS-CoV nsp16 (PDB 5YN5) and unbound SARS-CoV-2 nsp10 (PDB 6ZPE). Subsequently, we analyzed the interaction surface between MERS-CoV nsp16 and SARS-CoV-2 nsp10 (Fig. 1I), and then superimposed them onto the MERS-CoV nsp16/nsp10 complex (Fig. 1J). We observed a significant difference at the 58th residue of nsp10 (SARS-CoV-2, Thr; MERS-CoV, Lys); however, the residue interacting with the 58th residue of nsp10, Lys-89 of nsp16, was highly conserved across both viruses (Supplementary Fig. S2D–**F**).

We thus generated mutants of SARS-CoV-2 nsp10 T58K and MERS-CoV nsp10 K58T. The ^{3}H-methyl-incorporation assays suggested that the 2′-O-MTase activity of MERS-CoV nsp16 was partially inhibited when MERS-CoV nsp10 K58T was used as a cofactor, compared to SARS-CoV-2

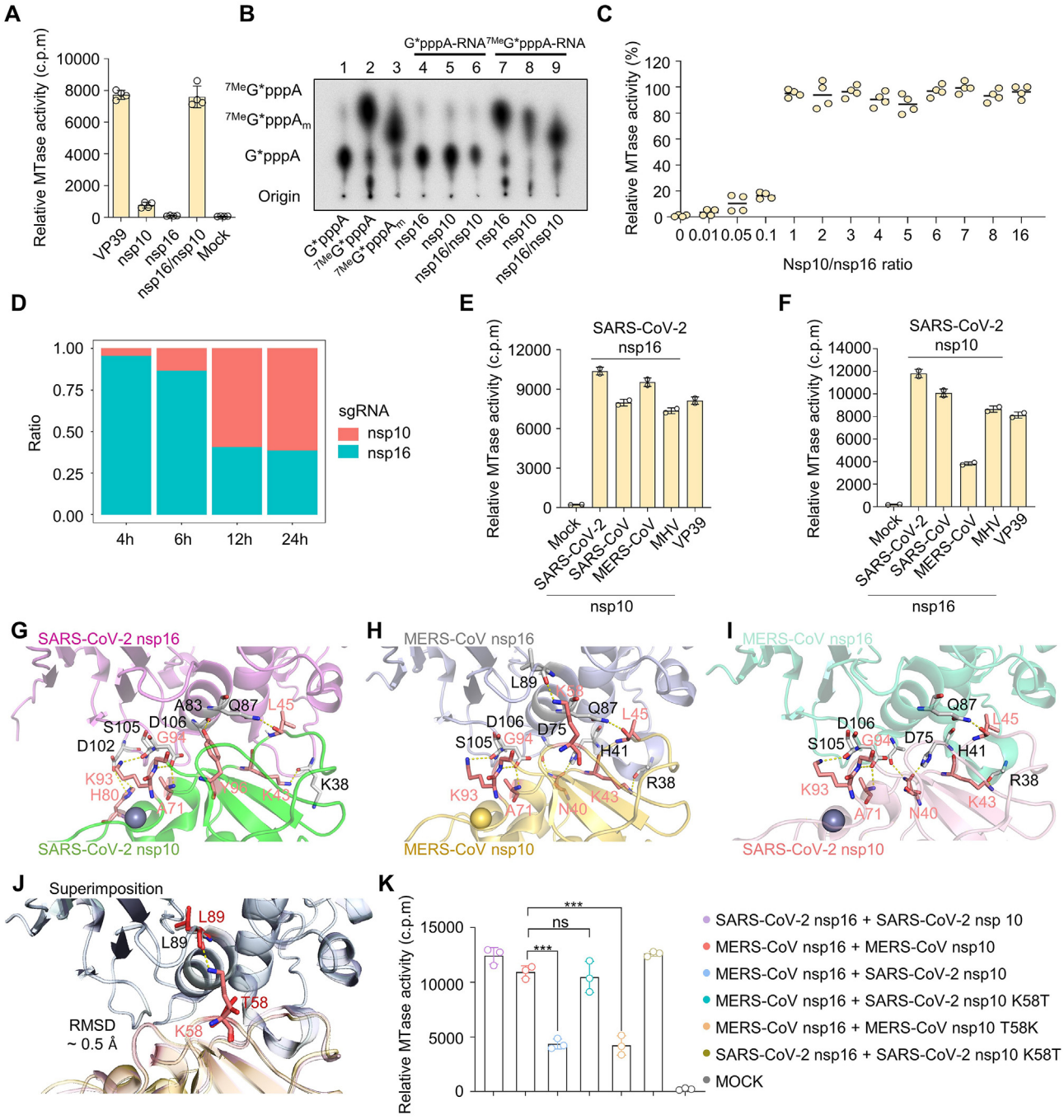

Fig. 1. Identification of SARS-CoV-2 2′-O-MTase activity. **A** Various proteins were employed in the ^{3}H–methyl-incorporation experiment, with the final concentration of proteins established at 1 μg. VP39 was utilized as the positive control and nsp5 served as a negative control (n = 4, mean values ± SD). **B** The ^{32}P-labeled RNA substrates (G*pppA-RNA and ^{7Me}G*pppA-RNA, lanes 4–9) were respectively reacted with nsp16, nsp10 and nsp16/nsp10 complex, following which the cap structure was released after digestion by nuclease P1, as analyzed by thin-layer chromatography (TLC). The markers G*pppA (lane1), ^{7Me}G*pppA (lane 2) and ^{7Me}G*pppA$_m$ (lane 3) were prepared with commercial Vaccinia virus capping enzymes. The positions of origin and migration of G*pppA, ^{7Me}G*pppA and ^{7Me}G*pppA$_m$ (lanes 1, 2 and 3) were indicated on the left. **C** The effect of nsp16/nsp10 ratio on 2′-O-MTase activity was investigated under the optimum conditions. Values at optimum nsp16/nsp10 ratios were arbitrarily set to 100% (n = 4, mean values ± SD). **D** Statistics of nsp16 and nsp10 sgRNA composition in Vero E6 infected with SARS-CoV-2 based on NGS reads. **E** 2′-O-MTase activity assays of SARS-CoV-2 nsp16 stimulated by the noncognate nsp10 (MHV, MERS-CoV, and SARS-CoV) (n = 2, mean values ± SD). **F** Assessment of 2′-O-MTase activity in noncognate nsp16 (MHV, MERS-CoV, and SARS-CoV) stimulated by the SARS-CoV-2 nsp10 (n = 2, mean values ± SD). VP39 was utilized as the positive control. **G–I** The interaction interface of SARS-CoV-2 nsp16/nsp10 complex (**G**, PDB 6WKS), MERS-CoV nsp16/nsp10 complex (**H**, PDB 5YN5) and MERS-CoV nsp16/SARS-CoV-2 nsp10 complex (**I**, produced by ZDOCK). The main chain of nsp16 (SARS-CoV-2, violet; MERS-CoV, light blue; ZDOCK, cyan) and nsp10 (SARS-CoV-2, green; MERS-CoV, yellow; ZDOCK, pink) were shown as cartoons. The interacting residues in nsp16 were colored by atoms (C: white, H: white, N: blue, O: red, S: bright orange) and the residues in nsp10 were colored by atoms (C: pink, H: white, N: blue, O: red, S: orange), presented as sticks. **J** Modeling the location of the 89th residue of nsp16 (ZDOCK, red; MERS-CoV, colored by atoms, C: white, H: white, N: blue, O: red, S: orange) and the 58th residue of nsp10 (ZDOCK, red; MERS-CoV, colored by atoms, C: pink, H: white, N: blue, O: red, S: orange). **K** Different non-structural proteins were used to test 2′-O-MTase activity (n = 3, mean values ± SD). The data were statistically analyzed using unpaired Student's *t*-test. ns, not significant; ***$P < 0.001$.

nsp10; however, when SARS-CoV-2 nsp10 T58K was used as a cofactor, the 2′-O-MTase activity of MERS-CoV nsp16 was restored to its wild-type level (Fig. 1K). This observation suggested that a substitution of a single residue in SARS-CoV-2 nsp10 (K58T) resulted in a restriction of functional activation of MERS-CoV nsp16. Taken together, these results strongly suggested that the mechanism of nsp10 stimulating nsp16 depended on the interaction of the conserved recognition motifs at the spatial conformation.

3.2. Nsp10 regulates the binding of nsp16 to the substrate RNA and SAM

The efficient function of MTase relies on the precise binding of the substrate acceptor RNA and the methyl donor SAM, as well as precise guidance (Chen et al., 2011). To assess the RNA-binding capacity of proteins and determine if nsp10 was necessary for RNA binding, we conducted pull-down assays using nickel-nitrilotriacetic acid (Ni-NTA) resin and ^{3}H-labeled RNAs (Fig. 2A and B). The results showed that only

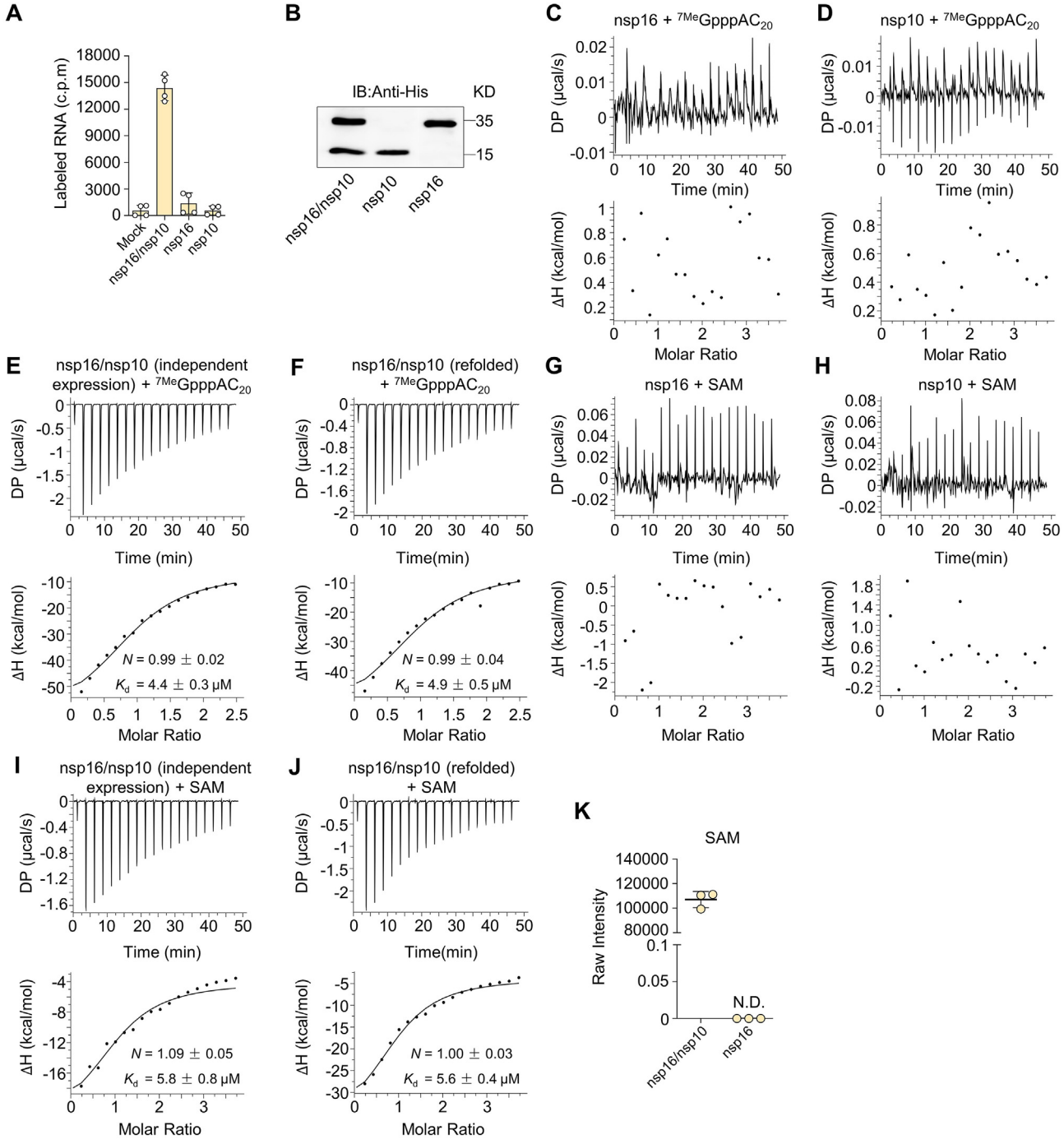

Fig. 2. Affinity analysis of SARS-CoV-2 nsp16/nsp10 for RNA or SAM binding. **A** The ^{3}H-labeled RNA substrate was used to assess the binding affinities towards nsp10, nsp16 and nsp16/nsp10 complex (n = 4, mean values ± SD). **B** 30 μL of the final suspensions from **A** were obtained and analyzed through Western Blotting. **C**–**F** Isothermal titration calorimetry (ITC) profiles revealed the binding affinity of the cap analog $^{7Me}GpppAC_{20}$ for nsp16 alone (**C**), nsp10 alone (**D**), as well as the binding affinity for the nsp16/nsp10 complex (independent expression, **E**; refolded, **F**). **G**–**J** ITC profiles for the binding affinity of S-adenosyl-L-methionine (SAM) towards nsp16 (**G**), nsp10 (**H**), and nsp16/nsp10 complex (independent expression, **I**; refolded, **J**). The top panels illustrated the raw data depicting sequential injections of $^{7Me}GpppAC_{20}$ (200 μM) or SAM (300 μM) into the indicated protein (15 μM). The bottom panels represented the plots of the heat evolved (kilocalories) per mole of $^{7Me}GpppAC_{20}$ or SAM. **K** LC-MS/MS metabolomic analysis identified differential metabolite (SAM) schematic representation. N.D., Not Detected.

pull-down of the nsp16 and nsp10 mixture gave rise to a high level of radioactive signal, whereas neither nsp16 nor nsp10 alone could bind RNA. We further measure the thermodynamic changes in RNA binding to proteins through ITC. The top image depicted the raw data concerning the titration of ^{7Me}Gppp-capped RNA (200 μM) towards nsp16, nsp10 and nsp16/nsp10 complex (15 μM). The bottom image illustrated the variations in enthalpy for each droplet of ^{7Me}Gppp-capped RNA throughout the system. According to the titration curve (Fig. 2C and D), the curves for single nsp16 or nsp10 with ^{7Me}Gppp-capped RNA fluctuated randomly around the 0-baseline. However, when adding ^{7Me}Gppp-capped RNA to nsp16/nsp10 complex was exothermic, it resulted in an exothermic reaction, indicated by a negative peak in the plots of power versus time (Fig. 2E and F). By fitting the data to a one set of sites model, we obtained the thermodynamic parameters for binding between the SARS-CoV-2 nsp16/nsp10 complex and ^{7Me}Gppp-capped RNA ($N = 0.99 \pm 0.02$ sites, $K_d = 4.4 \pm 0.3$ μM).

The results suggested that the binding of nsp16 to the substrate acceptor RNA was contingent upon the presence of nsp10. Similar, we utilize the ITC assay to evaluate the thermodynamic changes in SAM binding to proteins (Fig. 2G–I). The determination of the thermodynamic parameters for the binding of SARS-CoV-2 nsp16/nsp10 complex to SAM ($N = 1.09 \pm 0.05$ sites, $K_d = 5.8 \pm 0.8$ μM) was achieved (Fig. 2I). Neither nsp16 nor nsp10, when employed individually, exhibited the capacity to bind SAM (Fig. 2G and H). It is noteworthy that ITC methodology entailed the independent purification of nsp16 and nsp10 within *E. coli*, followed by their thorough *in vitro* amalgamation to form the complex. Prior studies have indicated that when nsp16/nsp10 is co-purified in *E. coli*, SAM binding pocket is often occupied by endogenous SAM (Brecher et al., 2015; Lin et al., 2020). As a result, it is common practice to subject the co-expressed nsp16/nsp10 complex from *E. coli* to a denaturation/refolding process during ITC experiments to evacuate occupied SAM. Intriguingly, we observed that the thermodynamic profiles acquired through this approach were congruent with the results when nsp16 and nsp10 are expressed individually and subsequently amalgamated to constitute the complex *in vitro* (Fig. 2E, F, 2I and 2J). Furthermore, by employing metabolomic mass spectrometry, we assessed the concentration of SAM in nsp16 or nsp16/nsp10 complex, revealing that nsp16 purified alone is incapable of binding with endogenous SAM in *E. coli* (Fig. 2K). Concurrently, via querying the data in the PDB bank for deposited crystal structures, we discovered that the crystal structure of nsp16 bound solely to SAM has not yet been identified (data not shown). Our findings underscored that neither SARS-CoV-2 nsp16 nor nsp10 can bind independently with SAM or RNA, aligning with the findings from most other coronaviruses.

In conclusion, the cofactor nsp10 facilitated the efficient binding of nsp16 to the substrate receptor RNA and the methyl donor SAM.

3.3. Biochemical characterization of 2′-O-methyltransferase

To accurately mimic the environment and conditions in which SARS-CoV-2 nsp16 performs 2′-O-MTase activity in the host, we further optimized and characterized its biochemical properties *in vitro*. We initially assessed the optimal temperature for the capping reaction (Fig. 3A). Our results suggested that 30 °C was the optimum temperature, which aligned with the findings from SARS-CoV and MERS-CoV (Bouvet et al., 2010; Aouadi et al., 2017). Interestingly, SARS-CoV-2 nsp16/nsp10 retained more than 50% 2′-O-MTase activity at 10 °C and 55 °C, which may be associated with the potential intermediate host of SARS-CoV-2 (Huang et al., 2021; Shi et al., 2020). We also characterized the optimal pH of nsp16, testing a pH gradient ranging from 3 to 12. As shown in Fig. 3B, 2′-O-MTase activity could not be detected in either strongly acidic or alkaline environments. The optimal pH for SARS-CoV-2 2′-O-MTase was found to be 7.0.

Previous evidence has shown that appropriate metal cations can promote methyltransferase activity (Decroly et al., 2008b; Jeffery and Roth, 1987). Therefore, four metal cations were performed to explore the cations capable of impacting 2′-O-MTase activity in SARS-CoV-2. As shown in Fig. 3C, compared to Mg^{2+}, Na^{+} and K^{+} potently enhanced the

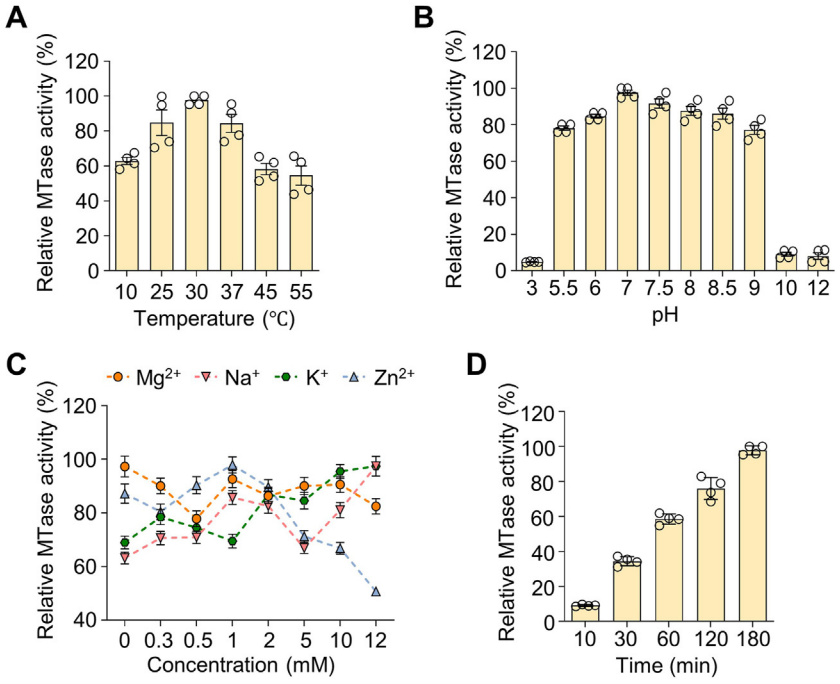

Fig. 3. Biochemical parameters associated with the 2′-O-MTase activity of SARS-CoV-2 nsp16/nsp10. **A–C** The 2′-O-MTase activities were detected across diverse temperatures (**A**), pH values (**B**) and various metal cations (**C**). The values at determined optima were set to 100%. The data represent two (**C**) or four (**A** and **B**) independent experiments. The error bars indicate standard deviations. **D** Time course of the methylation reaction was depicted. The reaction was terminated at the indicated time points by diluting the reaction mixture with a 10-fold excess of 20 mM ice-cold S-(5′-Adenosyl)-L homocysteine (SAH) (n = 4, mean values ± SD).

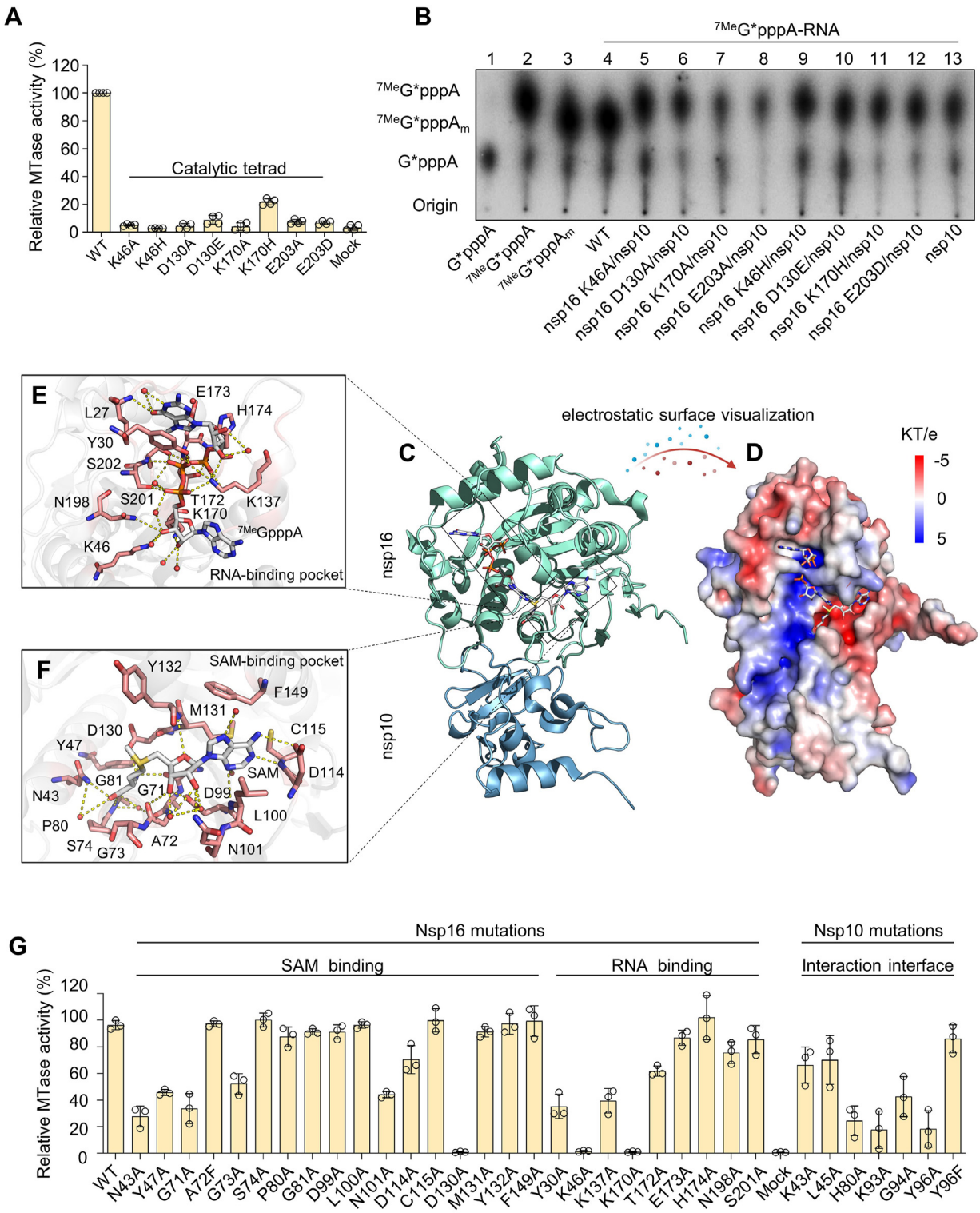

Fig. 4. Analysis of protein conformation and mutational effects on 2′-O-MTase activity of SARS-CoV-2 nsp16/nsp10 *in vitro*. **A** The 2′-O-MTase activity of nsp16 mutants associated with K-D-K-E motif was evaluated. The wild-type activity was defined as 100%. **B** The ^{32}P-labeled RNA substrates (^{7Me}*GpppA-RNA) reacted with related K-D-K-E nsp16 mutants. After nuclease P1 digestion, the released cap structure was detected and further analyzed via TLC assay (lanes 4–12). The positions of origin and migration of makers, G*pppA, ^{7Me}G*pppA and ^{7Me}G*pppA$_m$ (lanes 1, 2 and 3), were indicated on the left. **C** The overall structure of SARS-CoV-2 nsp16/nsp10 complex (PDB 6WKS, nsp16 in green, nsp10 in blue) was shown as a cartoon. SAM and ^{7Me}GpppA were depicted as a stick model colored by atoms (C: white, H: white, N: blue, O: red, S: yellow). **D** The surface of the nsp16/nsp10 was colored according to the electrostatic surface potential (level −5~5 KT/e). **E** and **F**, SAM-binding pocket and RNA-binding pocket of SARS-CoV-2 nsp16 were shown. All residues were presented as a stick model colored by atoms (C: salmon, H: white, N: blue, O: red, S: orange), and water were shown as red dots. **G** Related 2′-O-MTase activities of SARS-CoV-2 nsp16 mutants and nsp10 mutants were detected using ^{7Me}GpppAC$_{20}$ as the substrate in ^{3}H-methyl-incorporation assays. An activity of 100% corresponds to that of WT (n = 3, mean values ± SD).

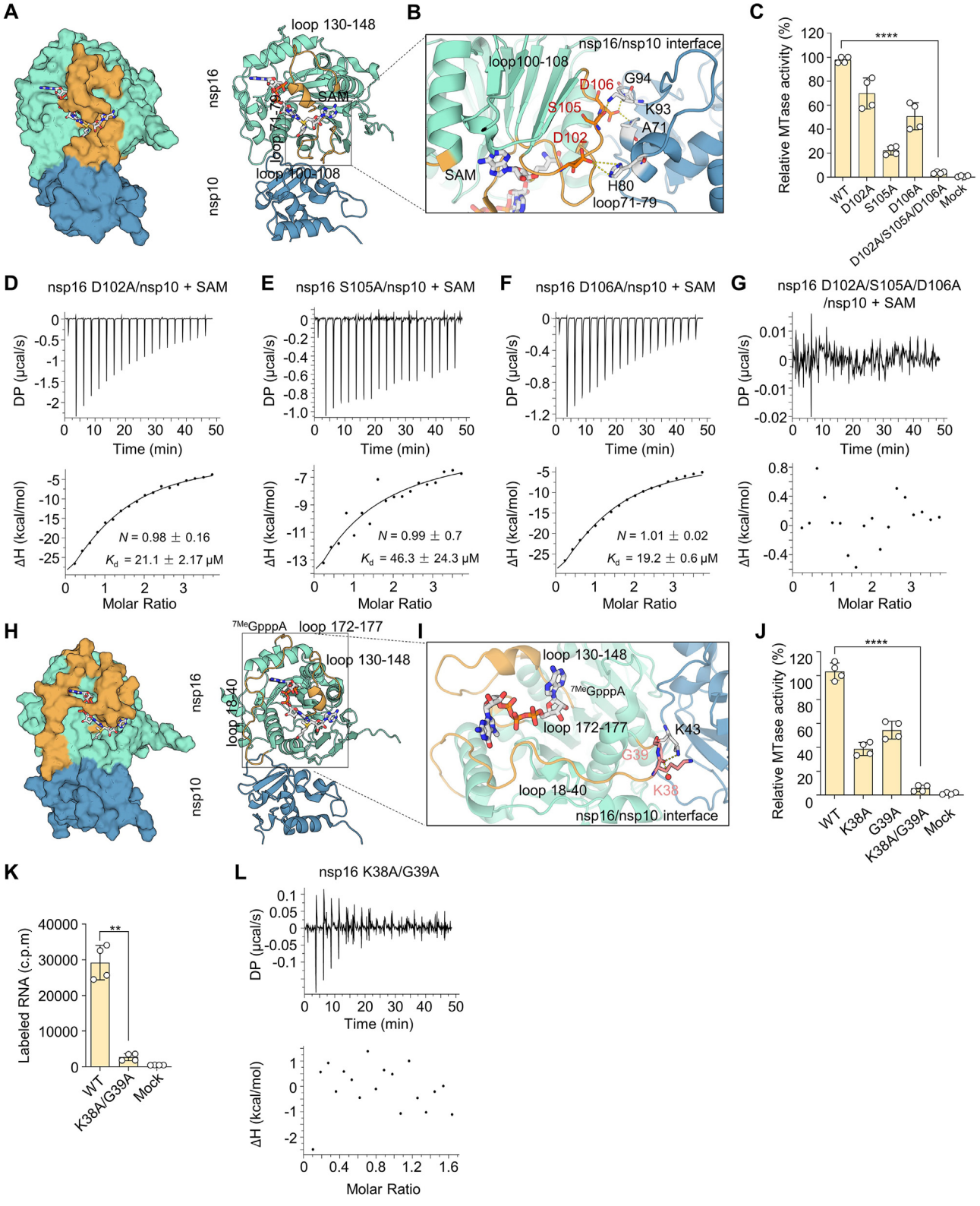

(caption on next page)

Fig. 5. Nsp10-mediated SAM binding mode and RNA binding pattern. **A** The overall structure of SARS-CoV-2 nsp16/nsp10 complex was shown as surface (left) or cartoon (right). Nsp10 was colored in blue, and nsp16 was colored in green. The loop 71–79, loop 100–108 and loop 130–148 regions were colored in yellow. SAM were depicted as stick and colored by atoms (C: white, H: white, N: blue, O: red, S: yellow). **B** Atomic detail of nsp10-mediated stabilization of the SAM-binding pocket. Residues Asp-102, Ser-105 and Asp-106 of nsp16 were shown as sticks and colored by atoms (C: orange, H: white, N: blue, O: red, S: bright orange). Residues Ala-71, His-80 and Lys-93 of nsp10 were shown as sticks and colored by atoms (C: white, H: white, N: blue, O: red, S: orange). Hydrogen bonds and salt bridges were shown as yellow dotted lines and red dotted lines, respectively. **C** Detection of 2′-O-MTase activities in wild type (WT) nsp16 and related mutants using ^{7Me}GpppAC$_{20}$ as the substrate. Nsp5 was used as a negative control (n = 4, mean values ± SD). **D**–**G** Binding affinity of SARS-CoV-2 nsp16 D102A/nsp10 (**D**), nsp16 S105A/nsp10 (**E**), nsp16 D106A/nsp10 (**F**) and nsp16 D102A/S105A/D106A/nsp10 (**G**) towards SAM, respectively, via ITC assay. The top panels depicted the raw data for sequential injections of SAM (300 μM) into indicated protein complex (15 μM). The bottom panels represented the plots of the heat evolved (kilocalories) per mole of SAM. **H** RNA-binding pocket were presented. The loop 18–40, loop 130–148, and loop 172–177 regions were colored in yellow. ^{7Me}GpppA were depicted as stick and colored by atoms (C: white, H: white, N: blue, O: red, S: yellow). **I** Atomic detail from (**H**). Residues Lys-38 and Gly-39 of nsp16 were shown as sticks and colored by atoms (C: pink, H: white, N: blue, O: red, S: bright orange). Residues Lys-43 of nsp10 were shown as sticks and colored by atoms (C: white, H: white, N: blue, O: red, S: orange). Hydrogen bonds were shown as yellow dotted lines. **J** Assessment of 2′-O-MTase activities in wild type nsp16 and related mutants. Nsp5 was used as a negative control (n = 4, mean values ± SD). **K** Evaluation of RNA binding affinity towards wild type or nsp16 K38A/G39A mutant (n = 4, mean values ± SD). **L** ITC profiles for the binding of nsp16 K38A/G39A to ^{7Me}GpppA-capped RNA. The data were statistically analyzed using unpaired Student's *t*-test with Welch's correction. ns, not significant; $^{**}P < 0.01$, $^{***}P < 0.001$, $^{****}P < 0.0001$.

2′-O-MTase activity at high concentrations. On the other hand, Zn^{2+} had a dual effect on the activity, with a significant increase at a concentration of 1 mM but a decrease at higher concentrations. Employing zinc fingers as a primary structural attribute, nsp10 has been demonstrated to play a crucial role in its biological function. This is attributed to the inherent property of zinc fingers as interaction modules, capable of binding with proteins, nucleic acids, and small molecules (Krishna et al., 2003). Intriguingly, certain MTases have previously been reported to be regulated through specific interactions with zinc finger domains (Pradhan et al., 2008; Shikauchi et al., 2009). Furthermore, the time course experiment demonstrated that the substrate accumulation gradually increased over a period of at least 3 h (Fig. 3D), indicating that the RNA capping reaction of SARS-CoV-2 was a continuous process under standard conditions. In summary, SARS-CoV-2 exhibited the maximum 2′-O-MTase activity at pH 7.0 and 30 °C in the presence of 1 mM Zn^{2+}.

3.4. Identification of critical residues in the MTase activity through structural analysis

The surface site and close-up view of K-D-K-E in the central groove of nsp16 were depicted (Supplementary Fig. S2G). It was observed that the K-D-K-E catalytic tetrad is located in the core of the protein, proximal to the SAM binding pocket and RNA binding pocket. To investigate the impact of the physicochemical properties of the catalytic tetrad on 2′-O-MTase activity, we constructed eight mutants, which are as follows: K46A, K46H, D130A, D130E, K170A, K170H, E203A, E203D (K, Lys; H, His; D, Asp; A, Ala; E, Glu). The results showed that, compared with wild type protein, the substitution of Alanine in K-D-K-E motif completely abolished the 2′-O-MTase activity. Upon substitution of K-D-K-E with amino acids with identical physical and chemical properties, only the K170H mutation exhibited partial restoration of 2′-O-MTase activity (Fig. 4A). TLC assay suggested that alterations in K-D-K-E motif could not modify ^{7Me}Gppp-capped RNA to form cap-1 structure (Fig. 4B). In conclusion, these findings indicated that K-D-K-E motif severed as the determinant of SARS-CoV-2 2′-O-MTase activity.

We calculated the electrostatic surface potential in terms of the overall structure (Fig. 4C). It was observed that the methyl donor SAM is situated in a negatively charged pocket, while the substrate acceptor RNA is positioned in a positively charged pocket (Fig. 4D). The first nucleoside, N^7-methylguanosine binds adjacent to the methyl donor SAM binding pocket. The dynamics and atomic details of the 2′-O-methylation of nsp16 are depicted. According to the crystal structure (PDB 6WKS), residues with polar contacts in the range of SAM~4 Å are presented: Asn-43, Tyr-47, Gly-71, Ala-72, Gly-73, Ser-74, Pro-80, Gly-81, Asp-99, Leu-100, Asn-101, Asp-114, Cys-115, Asp-130, Met-131, Tyr-132, Phe-149 (Fig. 4E). These amino acids establish a densely interconnected network through electrostatic forces, van der Waals forces, and hydrophobic interactions, thereby confining SAM into an extended conformation. We further resolved the residues that interacted with the receptor ^{7Me}GpppA via polar interactions: Leu-27, Tyr-30, Lys-46, Lys-137, Lys-170, Thr-172, Glu-173, His-174, Asn-198, Ser-201 (Fig. 4F). These specific residues dynamically regulate RNA binding through hydrogen bonds, hydrophobic interactions, and π-π superposition. Meanwhile, the biochemical analysis confirmed that in addition to K-D-K-E motif, residues Asn-43, Tyr-47, Gly-71, Gly-73, and Asn-101 of nsp16 played the critical roles in SAM binding, while residues Tyr-30, Lys-137 and Thr-172 of nsp16 corroborated the pivotal roles in RNA binding (Fig. 4G). Additionally, residues Lys-43, Lys-93, Tyr-96 of nsp10 were identified as pivotal in the interface. It has been previously reported that the substitution Y96F in nsp10 overstimulates the 2′-O-MTase activity of SARS-CoV nsp16 (Lugari et al., 2010); however, this phenotype was not observed in SARS-CoV-2 (Fig. 4G).

3.5. Structural and biochemical insights into the mechanism of SAM binding and RNA binding to nsp10/nsp16

The ligand SAM lies at the C-terminus similar to most SAM-dependent MTases (Martin and McMillan, 2002). Through the analysis of the crystal structure, we pay attention to several loop structures around the SAM. The crystal structure shows that the binding pocket of nsp16 consists of three loops: loop 71–79, loop 100–108, and loop 130–148 (Fig. 5A). These loops form a deep negatively charged groove that allows SAM to bind within the pocket. Additionally, the inherent flexibility of the loops also enhances the adaptability of the SAM binding pocket. Therefore, additional support from nsp10 is necessary to ensure the stability of SAM binding. This supports the findings that nsp16 alone is unable to exhibit 2′-O-MTase activity in the presence of SAM (Fig. 2G–J). Residues D102, S105, and D106 are in the loop region of the SAM binding pocket and contribute to the interacting interface (Fig. 5B). It is hypothesized that SARS-CoV-2 regulates the flexible loop structure through the interaction between nsp16 and nsp10, thereby stabilizing the SAM binding pocket and enhancing the SAM binding capacity. To validate this hypothesis, mutants of nsp16 were generated (D102A, S105A, D106A, and D102A/S105A/D106A), and the enzyme activity was evaluated *in vitro* (Fig. 5C). The results showed that any alteration in these residues resulted in attenuated 2′-O-MTase activity and the triple mutant completely abolished 2′-O-MTase activity. Moreover, ITC assay indicated that compared to wild type protein (K_d = 5.8 ± 0.8 μM) (Fig. 2I), D102A mutant (K_d = 21.1 ± 2.17 μM), S105A mutant (K_d = 46.3 ± 26.3 μM), and D106A mutant (K_d = 19.2 ± 0.6 μM) diminished the binding affinity of nsp16 to the methyl donor SAM, while the triple mutants virtually abolished nsp16 binding to SAM (Fig. 5D–G).

The RNA binding pocket filled with a negative charge is composed of loop 18–40, loop 130–148 and loop 172–177 regions (Fig. 4D, 5H). The presence of flexible loop allows for the accommodation of the RNA cap substrate, and enables a deep groove binding of the N^7-methyl guanosine base of Cap-0. Notably, the loop 18–40 regions extend toward the nsp16/nsp10 interaction interface, where Lys-38 and Gly-39 of nsp16 form a hydrogen bond with Lys-43 of nsp10 (Fig. 5I). Additionally, Lys-38 and Gly-39 form a β-turn element and leads to the reversal of nsp16 chain

orientation and the retraction of the binding pocket. We thus generated two single mutants (K38A, G39A) and a double mutant (K38A/G39A) at the interface of nsp16. The K38A mutant and G39A mutant attenuated by 60% and 50% the 2′-O-MTase activity, respectively, while the K38A/G39A mutant completely abrogated 2′-O-MTase activity (Fig. 5J). Furthermore, the K38A/G39A mutant completely disrupted the binding of the substrate ^{7Me}GpppAC$_{20}$ to the nsp16/nsp10 complex (Fig. 5K and L). Taken together, our findings suggested that the cofactor nsp10 exerts a traction on the flexible loop structure of SARS-CoV-2 by interacting with nsp16 residues, thereby stabilizing the binding pocket and facilitating precise binding of SAM and RNA to the nsp16/nsp10 complex.

3.6. Evaluation of inhibitors targeting 2′-O-MTase activity

With ongoing exploration of SAM-dependent methylation, it has been found that the viral MTase exhibits numerous original characteristics (Dong et al., 2008). Furthermore, various small molecules have been found to inhibit the viral MTase (Bouvet et al., 2010; Selisko et al., 2010; Zeng et al., 2016; Aouadi et al., 2017), providing a significant target site for the development of antiviral drug. To screen for potential compounds that exhibit inhibitory effects on SARS-CoV-2 2′-O-MTase, we employed isotope labeling techniques to establish a compound screening platform targeting 2′-O-MTase (Fig. 6A). A subset of compounds reported through computational simulation and bioinformatics analyses were initially investigated. These compounds included Raltegravir, Maraviroc, Prednisolone (Tazikeh-Lemeski et al., 2020), Phthalocyanine, Bemcentinib (Encinar and Menendez, 2020), Daphnetine, Telvivudine (Maurya et al., 2020), as well as some small molecules that showed significant effects on the activity of methyltransferase in other coronaviruses: S-(5′-Adenosyl)-L homocysteine (SAH), Sinefungin (SIN) (Decroly et al., 2008a; Zeng et al., 2016; Aouadi et al., 2017), Guanosine triphosphate (GTP), Ribavirin (RIBA) (Decroly et al., 2008a), ^{7Me}GpppA (Zeng et al., 2016; Aouadi et al., 2017), and Aurintricarboxylic acid (ATA) (Bouvet et al., 2010). All the compounds were tested at a concentration of 100 μM (Fig. 6B), and SIN, SAH and ^{7Me}GpppA showed obvious inhibitory activity.

Following the establishment of the concentration gradient, and the corresponding compound was further characterized to determine its half maximal inhibitory concentration (IC_{50}). Crystal structure analysis revealed that the conserved SAM binding pocket of SARS-CoV-2 could be targeted by SAM analogues, such as SIN (Lin et al., 2020; Krafcikova et al., 2020). SIN acts as an inhibitory agent by competitively binding to

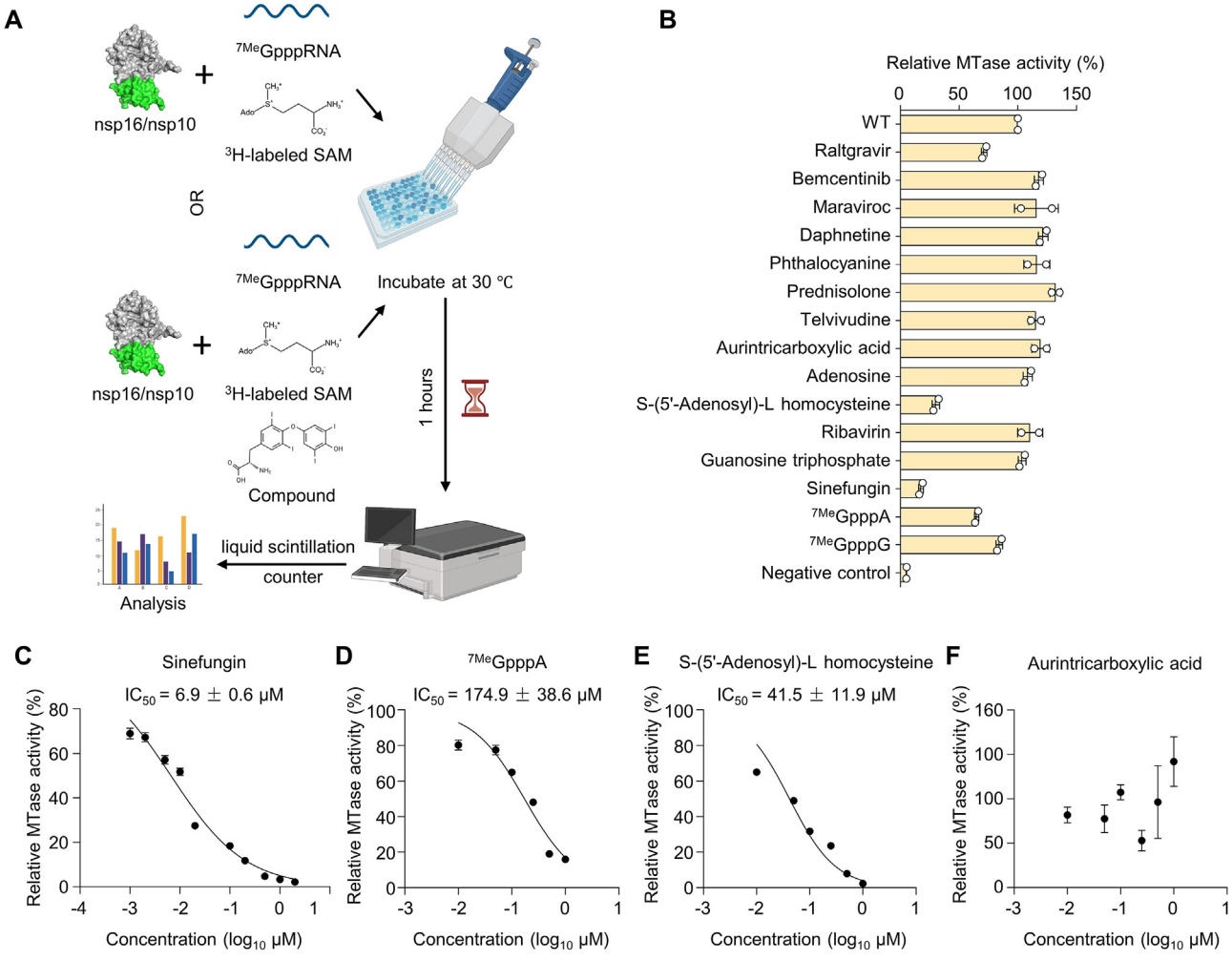

Fig. 6. Potential inhibitors screening of the SARS-CoV-2 2′-O-MTase activity. **A** Assessment scheme in a 96-well format. Figures were created and assembled using BioRender and Adobe illustration. **B** In the preliminary screening, all compounds were tested at a concentration of 100 μM, and the 2′-O-MTase activity in the group without inhibitors (WT) was considered as 100%. **C–F** Further characterization of potential inhibitors was performed based on the results from (Fig. 6B). The reaction mixtures were progressively supplemented with escalating concentrations of Sinefungin (**C**), ^{7Me}GpppA (**D**), S-(5′-Adenosyl)-L homocysteine (**E**), and Aurintricarboxylic acid (**F**), and the 2′-O-MTase activity was subsequently quantified. The 2′-O-MTase activity in the group without inhibitors (WT) was defined as 100%. The data were further analyzed utilizing GraphPad to determine the half maximal inhibitory concentration (IC_{50}) of each compound.

the pocket. Our results confirmed that SIN showed a robust inhibition profile on 2′-O-MTase with IC_{50} values of 6.9 μM (Fig. 6C). The cap analogues ^{7Me}GpppA is a competitive inhibitor specifically designed to obstruct the RNA cap-0 binding site. The IC_{50} of ^{7Me}GpppA was 174.9 μM (Fig. 6D). The inhibitory effect of SAH on SARS-CoV-2 2′-O-MTase was also evaluated (IC_{50} = 41.5 μM) (Fig. 6E), demonstrating its potency as a suppressor of the MTase family, as previously reported (Pugh and Borchardt, 1982). Of interest, ATA is a potent inhibitor of SARS-CoV nsp16/nsp10 2′-O-MTase activity (Bouvet et al., 2010), however, it showed no inhibitory effect on SARS-CoV-2 (Fig. 6F). In a word, SIN, ^{7Me}GpppA and SAH exhibited a significant inhibitory effect on SARS-CoV-2 2′-O-MTase activity.

4. Discussion

In this study, we found that SARS-CoV-2 nsp16 exhibited SAM-dependent 2′-O-MTase activity in the presence of nsp10, as demonstrated by comprehensive biochemical experiments. These findings align with previous studies on coronaviruses, despite the dissimilar sequence similarity of nsp16 and their phylogenetic relationship (Aouadi et al., 2017; Decroly et al., 2008a, 2011a; Selisko et al., 2010). Surprisingly, subsequent assessments revealed a significant decrease in the dependence of SARS-CoV-2 nsp16 on cofactor nsp10, while maintaining 2′-O-MTase activity (Fig. 1). Possible explanations for this phenomenon could lie in the optimal conformation and strategic readjustments. Notably, we have previously shown that stimulation of nsp16 2′-O-MTase activity by nsp10 is a universal and conserved mechanism in coronaviruses, and that nsp10 is functionally interchangeable in the stimulation of nsp16 of different coronaviruses (Wang et al., 2015). Our study on SARS-CoV-2 serves as an important extension and supplement to this conclusion. In the investigation of SARS-CoV, structural analysis of nsp10 in its non-ligand form and in its complex with nsp16 demonstrated that the conformation of nsp10 remained largely unchanged following its combination with nsp16 (Joseph et al., 2006). A comparison of unbound nsp10 and nsp10 bound to nsp16 in SARS-CoV-2 revealed a slight rearrangement only in the loop 1 region due to nsp14 binding adaptation (Rogstam et al., 2020). Our study conducted a series of primary amino acid sequence alignments and structural superpositions, confirming that SARS-CoV-2 nsp10 shared strong similarities with various coronaviruses. Additionally, we found that the nsp16/nsp10 interface was highly conserved, potentially explaining the cross-reactivity between nsp10 and nsp16 across different coronaviruses.

A significant body of prior studies has confirmed that coronavirus nsp16 possesses a highly conserved K-D-K-E tetrad, which serves as a catalytic center. This tetrad facilitates the execution of an S_N2-reaction-mediated 2′-O-MTase (Hodel et al., 1998; Decroly et al., 2008a; Hager et al., 2002; Zhou et al., 2007). SAM and RNA, acting as methyl donor and receptor for methylation, are extended to the surface through K-D-K-E motif. This suggested that the K-D-K-E motif is involved in SAM binding and RNA binding networks. Mutation analysis demonstrated that any alteration in the K-D-K-E motif, including changes in charge, spatial configuration, polarity, and physicochemical properties, could irreversibly impair the functional activity of nsp16. Using this property, Russ A. et al. and Schindewolf C. et al. constructed a chimeric virus with K-D-K-E mutation of nsp16, confirming the significance of 2′-O-methyltransferase in innate antiviral immunity *in vivo* (Schindewolf et al., 2023; Russ et al., 2022). Ye Z.W. et al. generated a recombinant SARS-CoV-2 strain carrying the nsp16 D130A mutation, demonstrating the potential of nsp16 inactivation as a strategy for developing live attenuated SARS-CoV-2 vaccines. (Ye et al., 2022). In addition, the nsp16/nsp10 complex exhibited strong steric stability. In particular, a single substitution in nsp16 affected the SAM binding affinity of the nsp16/nsp10 complex while concurrently maintaining the overall conformational stability and functionality (Fig. 4). This represents another manifestation of the strategic shift in SARS-CoV-2.

The nsp16 binding cleft, which accommodates methyl donor SAM and substrate macromolecular RNA, is a spacious and deep groove, necessitating robust adjustability and flexibility. The existence of loop gates has paved the way for achieving this goal. Based on our observations, we propose a unique mechanism of SARS-CoV-2 nsp16/nsp10 complex binding to SAM and RNA: SARS-CoV-2 regulates the flexible loop structure through the interaction between specific residues within nsp16 and nsp10, thereby widening and stabilizing the binding pocket. The electrostatic epitopes generated by the variable loop structure bind SAM and RNA substrates in distinct pockets, facilitating a well-coordinated capping process. The unique mechanism and flexible conformational change of SARS-CoV-2 nsp16 enable it to require only one nsp10 to maximize methyltransferase activity (1:1), contrasting with SARS-CoV nsp16 which necessitates at least six nsp10 (1:6) (Bouvet et al., 2010).

The critical role of cap structure and the intricate capping process of mRNA provide numerous potential targets and insights for the design of drugs and vaccines (Chrebet et al., 2005; Decroly et al., 2011b; Ferron et al., 2012; Schwer et al., 2001; Woyciniuk et al., 1995). Compared with previously reported results, SIN showed similar inhibitory effects against 2′-O-MTase of SARS-COV-2 (IC_{50} = 6.9 μM) and MERS-CoV (IC_{50} = 7.4 μM) (Aouadi et al., 2017). The inhibitory effect on GAV 2′-O-MTase is relatively mild (IC_{50} = 28.7 μM) (Zeng et al., 2016), whereas the inhibitory effect on SARS-CoV, dengue virus 2′-O-MTase is more potent (IC_{50} = 736 nM and 630 nM) (Selisko et al., 2010; Decroly et al., 2008a). These results implied that nsp16 from different viruses have varying discrimination abilities towards SAM and its analogues. Moreover, ITC data from Lin S. et al. showed that SIN binds to SARS-CoV-2 nsp16/nsp10 (K_d = 13.7 ± 2.3 μM) with an over three-fold lower affinity than SAM (K_d = 4.1 ± 0.4 μM) (Lin et al., 2020). Together, although the various SAM-dependent MTase had similar organizational structures, nsp16 could potentially evolve a distinct variant at the conserved SAM binding site.

The primary constraint of this investigation is that, although we ascertained that SAH, SFG, and other compounds can suppress the MTase activity of SARS-CoV-2 nsp16, these substances do not qualify as optimal antiviral agents due to their non-specific inhibitory action. Previous studies have demonstrated that a short peptide can specifically inhibit 2′-O-MTase activity by interfering with the interaction between nsp10 and nsp16 of SARS-CoV (Ke et al., 2012). Immunogenic disruption of the nsp16-nsp10 interface has also been shown to protect mice from other lethal attacks (Daffis et al., 2010; Zust et al., 2011). Therefore, drugs targeting coronavirus nsp16/nsp10 interaction epitopes deserve further study.

5. Conclusion

In summary, our study comprehensively characterized the biochemical properties of the SARS-CoV-2 2′-O-MTase *in vitro*. We provided functional and mechanistic insights into the 2′-O-MTase of the virus. This unique capping mechanism has enabled us to understand the precise process of 2′-O-methylaition of virus. These findings offer theoretical basis underpinning for the advancement of broad-spectrum antiviral medications.

Data availability

All data supporting the conclusions of this study are reported in the paper. The raw data are available from the corresponding author with no restrictions upon reasonable request.

Ethics statement

This article does not contain any studies with human or animal subjects performed by any authors.

Author contributions

Jikai Deng: Conceptualization, Methodology, Software, Validation, Investigation, Data Curation, Writing-Original Draft preparation, Writing-Review & Editing. Gongfei Yu: Software, Validation, Investigation, Data Curation, Writing-Original Draft preparation, Writing-Review & Editing. Yingjian Li: Conceptualization, Methodology, Validation. Xue Tan: Validation, Investigation, Formal analysis. Xuemei Liu: Data curation, Writing – review & editing. Shimin yang: Methodology, Software, Data Curation. Xianying Chen: Methodology, Resources. Hongyun Wang: Methodology, Resources. Qianyun Liu: Methodology, Resources. Chao Shen: Resources. Li Zhou: Supervision, Project administration. Yu Chen: Conceptualization, Supervision, Project administration, Funding acquisition, Writing-Review & Editing. All authors have read and agreed to the version of the manuscript.

Declaration of competing interest

All authors declare that there are no competing interests.

Acknowledgments

We would like to thank all the members of the laboratory for their valuable suggestions and technical support for this project. This study was supported by grants from the National Natural Science Foundation of China (82372223 and 82172243), the National Key R&D Program of China (2021YFF0702004), and the Fundamental Research Funds for the Central Universities of China (2042022dx0003).

Appendix A. Supplementary data

Supplementary data to this article can be found online at https://doi.org/10.1016/j.virs.2024.07.001.

References

Ahola, T., Laakkonen, P., Vihinen, H., Kaariainen, L., 1997. Critical residues of Semliki Forest virus RNA capping enzyme involved in methyltransferase and guanylyltransferase-like activities. J. Virol. 71, 392–397.

Aouadi, W., Blanjoie, A., Vasseur, J.J., Debart, F., Canard, B., Decroly, E., 2017. Binding of the methyl donor S-Adenosyl-l-Methionine to Middle East respiratory syndrome coronavirus 2'-O-methyltransferase nsp16 promotes recruitment of the allosteric activator nsp10. J. Virol. 91, e02217-16.

Bouvet, M., Debarnot, C., Imbert, I., Selisko, B., Snijder, E.J., Canard, B., Decroly, E., 2010. In vitro reconstitution of SARS-coronavirus mRNA cap methylation. PLoS Pathog. 6, e1000863.

Brecher, M.B., Li, Z., Zhang, J., Chen, H., Lin, Q., Liu, B., Li, H., 2015. Refolding of a fully functional flavivirus methyltransferase revealed that S-adenosyl methionine but not S-adenosyl homocysteine is copurified with flavivirus methyltransferase. Protein Sci. 24, 117–128.

Chen, Y., Cai, H., Pan, J., Xiang, N., Tien, P., Ahola, T., Guo, D., 2009. Functional screen reveals SARS coronavirus nonstructural protein nsp14 as a novel cap N7 methyltransferase. Proc. Natl. Acad. Sci. U. S. A. 106, 3484–3489.

Chen, Y., Guo, D., 2016. Molecular mechanisms of coronavirus RNA capping and methylation. Virol. Sin. 31, 3–11.

Chen, Y., Liu, Q., Guo, D., 2020. Emerging coronaviruses: genome structure, replication, and pathogenesis. J. Med. Virol. 92, 418–423.

Chen, Y., Liu, Q., Zhou, L., Zhou, Y., Yan, H., Lan, K., 2022. Emerging SARS-CoV-2 variants: why, how, and what's next? Cell Insight 1, 100029.

Chen, Y., Su, C., Ke, M., Jin, X., Xu, L., Zhang, Z., Wu, A., Sun, Y., Yang, Z., Tien, P., Ahola, T., Liang, Y., Liu, X., Guo, D., 2011. Biochemical and structural insights into the mechanisms of SARS coronavirus RNA ribose 2'-O-methylation by nsp16/nsp10 protein complex. PLoS Pathog. 7, e1002294.

Chrebet, G.L., Wisniewski, D., Perkins, A.L., Deng, Q., Kurtz, M.B., Marcy, A., Parent, S.A., 2005. Cell-based assays to detect inhibitors of fungal mRNA capping enzymes and characterization of sinefungin as a cap methyltransferase inhibitor. J. Biomol. Screen 10, 355–364.

Daffis, S., Szretter, K.J., Schriewer, J., Li, J., Youn, S., Errett, J., Lin, T.Y., Schneller, S., Zust, R., Dong, H., Thiel, V., Sen, G.C., Fensterl, V., Klimstra, W.B., Pierson, T.C., Buller, R.M., Gale Jr., M., Shi, P.Y., Diamond, M.S., 2010. 2'-O methylation of the viral mRNA cap evades host restriction by IFIT family members. Nature 468, 452–456.

Decroly, E., Debarnot, C., Ferron, F., Bouvet, M., Coutard, B., Imbert, I., Gluais, L., Papageorgiou, N., Sharff, A., Bricogne, G., Ortiz-Lombardia, M., Lescar, J., Canard, B., 2011a. Crystal structure and functional analysis of the SARS-coronavirus RNA cap 2'-O-methyltransferase nsp10/nsp16 complex. PLoS Pathog. 7, e1002059.

Decroly, E., Ferron, F., Lescar, J., Canard, B., 2011b. Conventional and unconventional mechanisms for capping viral mRNA. Nat. Rev. Microbiol. 10, 51–65.

Decroly, E., Imbert, I., Coutard, B., Bouvet, M., Selisko, B., Alvarez, K., Gorbalenya, A.E., Snijder, E.J., Canard, B., 2008a. Coronavirus nonstructural protein 16 is a cap-0 binding enzyme possessing (nucleoside-2'O)-methyltransferase activity. J. Virol. 82, 8071–8084.

Decroly, E., Imbert, I., Coutard, B., Bouvet, M.L., Selisko, B., Alvarez, K., Gorbalenya, A.E., Snijder, E.J., Canard, B., 2008b. Coronavirus nonstructural protein 16 is a cap-0 binding enzyme possessing (nucleoside-2'O)-methyltransferase activity. J. Virol. 82, 8071–8084.

Deng, J., Yang, S., Li, Y., Tan, X., Liu, J., Yu, Y., Ding, Q., Fan, C., Wang, H., Chen, X., Liu, Q., Guo, X., Gong, F., Zhou, L., Chen, Y., 2024. Natural evidence of coronaviral 2'-O-methyltransferase activity affecting viral pathogenesis via improved substrate RNA binding. Signal Transduct. Targeted Ther. 9, 140.

Dong, H., Zhang, B., Shi, P.Y., 2008. Flavivirus methyltransferase: a novel antiviral target. Antivir. Res. 80, 1–10.

Encinar, J.A., Menendez, J.A., 2020. Potential drugs targeting early innate immune evasion of SARS-coronavirus 2 via 2'-O-methylation of viral RNA. Viruses 12, 525.

Ferron, F., Decroly, E., Selisko, B., Canard, B., 2012. The viral RNA capping machinery as a target for antiviral drugs. Antivir. Res. 96, 21–31.

Hager, J., Staker, B.L., Bugl, H., Jakob, U., 2002. Active site in RrmJ, a heat shock-induced methyltransferase. J. Biol. Chem. 277, 41978–41986.

Hodel, A.E., Gershon, P.D., Quiocho, F.A., 1998. Structural basis for sequence-nonspecific recognition of 5'-capped mRNA by a cap-modifying enzyme. Mol. Cell 1, 443–447.

Hornung, V., Ellegast, J., Kim, S., Brzozka, K., Jung, A., Kato, H., Poeck, H., Akira, S., Conzelmann, K.K., Schlee, M., Endres, S., Hartmann, G., 2006. 5'-Triphosphate RNA is the ligand for RIG-I. Science 314, 994–997.

Huang, Y., Xie, J., Guo, Y., Sun, W., He, Y., Liu, K., Yan, J., Tao, A., Zhong, N., 2021. SARS-CoV-2: origin, intermediate host and allergenicity features and hypotheses. Healthcare (Basel) 9, 1132.

Ivanov, K.A., Ziebuhr, J., 2004. Human coronavirus 229E nonstructural protein 13: characterization of duplex-unwinding, nucleoside triphosphatase, and RNA 5'-triphosphatase activities. J. Virol. 78, 7833–7838.

Jeffery, D.R., Roth, J.A., 1987. Kinetic reaction-mechanism for magnesium binding to membrane-bound and soluble catechol O-methyltransferase. Biochemistry 26, 2955–2958.

Joseph, J.S., Saikatendu, K.S., Subramanian, V., Neuman, B.W., Brooun, A., Griffith, M., Moy, K., Yadav, M.K., Velasquez, J., Buchmeier, M.J., Stevens, R.C., Kuhn, P., 2006. Crystal structure of nonstructural protein 10 from the severe acute respiratory syndrome coronavirus reveals a novel fold with two zinc-binding motifs. J. Virol. 80, 7894–7901.

Ke, M., Chen, Y., Wu, A., Sun, Y., Su, C., Wu, H., Jin, X., Tao, J., Wang, Y., Ma, X., Pan, J.A., Guo, D., 2012. Short peptides derived from the interaction domain of SARS coronavirus nonstructural protein nsp10 can suppress the 2'-O-methyltransferase activity of nsp10/nsp16 complex. Virus Res. 167, 322–328.

Krafcikova, P., Silhan, J., Nencka, R., Boura, E., 2020. Structural analysis of the SARS-CoV-2 methyltransferase complex involved in RNA cap creation bound to sinefungin. Nat. Commun. 11, 3717.

Krishna, S.S., Majumdar, I., Grishin, N.V., 2003. Structural classification of zinc fingers: survey and summary. Nucleic Acids Res. 31, 532–550.

Lin, S., Chen, H., Ye, F., Chen, Z., Yang, F., Zheng, Y., Cao, Y., Qiao, J., Yang, S., Lu, G., 2020. Crystal structure of SARS-CoV-2 nsp10/nsp16 2'-O-methylase and its implication on antiviral drug design. Signal Transduct. Targeted Ther. 5, 131.

Liu, H., Kiledjian, M., 2006. Decapping the message: a beginning or an end. Biochem. Soc. Trans. 34, 35–38.

Lugari, A., Betzi, S., Decroly, E., Bonnaud, E., Hermant, A., Guillemot, J.C., Debarnot, C., Borg, J.P., Bouvet, M., Canard, B., Morelli, X., Lecine, P., 2010. Molecular mapping of the RNA Cap 2'-O-methyltransferase activation interface between severe acute respiratory syndrome coronavirus nsp10 and nsp16. J. Biol. Chem. 285, 33230–33241.

Mahalapbutr, P., Kongtaworn, N., Rungrotmongkol, T., 2020. Structural insight into the recognition of S-adenosyl-L-homocysteine and sinefungin in SARS-CoV-2 Nsp16/Nsp10 RNA cap 2'-O-Methyltransferase. Comput. Struct. Biotechnol. J. 18, 2757–2765.

Martin, J.L., Mcmillan, F.M., 2002. SAM (dependent) I AM: the S-adenosylmethionine-dependent methyltransferase fold. Curr. Opin. Struct. Biol. 12, 783–793.

Maurya, S.K., Maurya, A.K., Mishra, N., Siddique, H.R., 2020. Virtual screening, ADME/T, and binding free energy analysis of anti-viral, anti-protease, and anti-infectious compounds against NSP10/NSP16 methyltransferase and main protease of SARS CoV-2. J. Recept. Signal Transduct. Res. 40, 605–612.

Nallagatla, S.R., Toroney, R., Bevilacqua, P.C., 2008. A brilliant disguise for self RNA: 5'-end and internal modifications of primary transcripts suppress elements of innate immunity. RNA Biol. 5, 140–144.

Park, G.J., Osinski, A., Hernandez, G., Eitson, J.L., Majumdar, A., Tonelli, M., Henzler-Wildman, K., Pawlowski, K., Chen, Z., Li, Y., Schoggins, J.W., Tagliabracci, V.S., 2022. The mechanism of RNA capping by SARS-CoV-2. Nature 609, 793–800.

Pierce, B.G., Wiehe, K., Hwang, H., Kim, B.H., Vreven, T., Weng, Z., 2014. ZDOCK server: interactive docking prediction of protein-protein complexes and symmetric multimers. Bioinformatics 30, 1771–1773.

Pradhan, M., Esteve, P.O., Chin, H.G., Samaranayke, M., Kim, G.D., Pradhan, S., 2008. CXXC domain of human DNMT1 is essential for enzymatic activity. Biochemistry 47, 10000–10009.

Pugh, C.S., Borchardt, R.T., 1982. Effects of S-adenosylhomocysteine analogues on vaccinia viral messenger ribonucleic acid synthesis and methylation. Biochemistry 21, 1535–1541.

Ray, D., Shah, A., Tilgner, M., Guo, Y., Zhao, Y., Dong, H., Deas, T.S., Zhou, Y., Li, H., Shi, P.Y., 2006. West Nile virus 5'-cap structure is formed by sequential guanine N-7 and ribose 2'-O methylations by nonstructural protein 5. J. Virol. 80, 8362–8370.

Rehwinkel, J., Tan, C.P., Goubau, D., Schulz, O., Pichlmair, A., Bier, K., Robb, N., Vreede, F., Barclay, W., Fodor, E., Reis E Sousa, C., 2010. RIG-I detects viral genomic RNA during negative-strand RNA virus infection. Cell 140, 397–408.

Robert, X., Gouet, P., 2014. Deciphering key features in protein structures with the new ENDscript server. Nucleic Acids Res. 42, W320–W324.

Rogstam, A., Nyblom, M., Christensen, S., Sele, C., Talibov, V.O., Lindvall, T., Rasmussen, A.A., Andre, I., Fisher, Z., Knecht, W., Kozielski, F., 2020. Crystal structure of non-structural protein 10 from severe acute respiratory syndrome coronavirus-2. Int. J. Mol. Sci. 21, 7375.

Rosas-Lemus, M., Minasov, G., Shuvalova, L., Inniss, N.L., Kiryukhina, O., Brunzelle, J., Satchell, K.J.F., 2020. High-resolution structures of the SARS-CoV-2 2'-O-methyltransferase reveal strategies for structure-based inhibitor design. Sci. Signal. 13, eabe1202.

Russ, A., Wittmann, S., Tsukamoto, Y., Herrmann, A., Deutschmann, J., Lagisquet, J., Ensser, A., Kato, H., Gramberg, T., 2022. Nsp16 shields SARS-CoV-2 from efficient MDA5 sensing and IFIT1-mediated restriction. EMBO Rep. 23, e55648.

Schindewolf, C., Lokugamage, K., Vu, M.N., Johnson, B.A., Scharton, D., Plante, J.A., Kalveram, B., Crocquet-Valdes, P.A., Sotcheff, S., Jaworski, E., Alvarado, R.E., Debbink, K., Daugherty, M.D., Weaver, S.C., Routh, A.L., Walker, D.H., Plante, K.S., Menachery, V.D., 2023. SARS-CoV-2 Uses nonstructural protein 16 to evade restriction by IFIT1 and IFIT3. J. Virol. 97, e0153222.

Schwer, B., Lehman, K., Saha, N., Shuman, S., 2001. Characterization of the mRNA capping apparatus of Candida albicans. J. Biol. Chem. 276, 1857–1864.

Selisko, B., Peyrane, F.F., Canard, B., Alvarez, K., Decroly, E., 2010. Biochemical characterization of the (nucleoside-2'O)-methyltransferase activity of dengue virus protein NS5 using purified capped RNA oligonucleotides (7Me)GpppAC(n) and GpppAC(n). J. Gen. Virol. 91, 112–121.

Shi, J., Wen, Z., Zhong, G., Yang, H., Wang, C., Huang, B., Liu, R., He, X., Shuai, L., Sun, Z., Zhao, Y., Liu, P., Liang, L., Cui, P., Wang, J., Zhang, X., Guan, Y., Tan, W., Wu, G., Chen, H., Bu, Z., 2020. Susceptibility of ferrets, cats, dogs, and other domesticated animals to SARS-coronavirus 2. Science 368, 1016–1020.

Shikauchi, Y., Saiura, A., Kubo, T., Niwa, Y., Yamamoto, J., Murase, Y., Yoshikawa, H., 2009. SALL3 interacts with DNMT3A and shows the ability to inhibit CpG island methylation in hepatocellular carcinoma. Mol. Cell Biol. 29, 1944–1958.

Smith, E.C., Case, J.B., Blanc, H., Isakov, O., Shomron, N., Vignuzzi, M., Denison, M.R., 2015. Mutations in coronavirus nonstructural protein 10 decrease virus replication fidelity. J. Virol. 89, 6418–6426.

Tazikeh-Lemeski, E., Moradi, S., Raoufi, R., Shahlaei, M., Janlou, M.A.M., Zolghadri, S., 2020. Targeting SARS-COV-2 non-structural protein 16: a virtual drug repurposing study. J. Biomol. Struct. Dyn. 39, 4633–4646.

Viswanathan, T., Arya, S., Chan, S.H., Qi, S., Dai, N., Misra, A., Park, J.G., Oladunni, F., Kovalskyy, D., Hromas, R.A., Martinez-Sobrido, L., Gupta, Y.K., 2020. Structural basis of RNA cap modification by SARS-CoV-2. Nat. Commun. 11, 3718.

Wang, D., Jiang, A., Feng, J., Li, G., Guo, D., Sajid, M., Wu, K., Zhang, Q., Ponty, Y., Will, S., Liu, F., Yu, X., Li, S., Liu, Q., Yang, X.L., Guo, M., Li, X., Chen, M., Shi, Z.L., Lan, K., Chen, Y., Zhou, Y., 2021. The SARS-CoV-2 subgenome landscape and its novel regulatory features. Mol. Cell 81, 2135–2147.e5.

Wang, Y., Sun, Y., Wu, A., Xu, S., Pan, R., Zeng, C., Jin, X., Ge, X., Shi, Z., Ahola, T., Chen, Y., Guo, D., 2015. Coronavirus nsp10/nsp16 methyltransferase can Be targeted by nsp10-derived peptide in vitro and in vivo to reduce replication and pathogenesis. J. Virol. 89, 8416–8427.

Wilamowski, M., Sherrell, D.A., Minasov, G., Kim, Y., Shuvalova, L., Lavens, A., Chard, R., Maltseva, N., Jedrzejczak, R., Rosas-Lemus, M., Saint, N., Foster, I.T., Michalska, K., Satchell, K.J.F., Joachimiak, A., 2021. 2'-O methylation of RNA cap in SARS-CoV-2 captured by serial crystallography. Proc. Natl. Acad. Sci. U. S. A. 118, e2100170118.

Woyciniuk, P., Linder, M., Scholtissek, C., 1995. The methyltransferase inhibitor Neplanocin A interferes with influenza virus replication by a mechanism different from that of 3-deazaadenosine. Virus Res. 35, 91–99.

Yan, L., Ge, J., Zheng, L., Zhang, Y., Gao, Y., Wang, T., Huang, Y., Yang, Y., Gao, S., Li, M., Liu, Z., Wang, H., Li, Y., Chen, Y., Guddat, L.W., Wang, Q., Rao, Z., Lou, Z., 2021a. Cryo-EM structure of an extended SARS-CoV-2 replication and transcription complex reveals an intermediate state in cap synthesis. Cell 184, 184–193. e10.

Yan, L., Yang, Y., Li, M., Zhang, Y., Zheng, L., Ge, J., Huang, Y.C., Liu, Z., Wang, T., Gao, S., Zhang, R., Huang, Y.Y., Guddat, L.W., Gao, Y., Rao, Z., Lou, Z., 2021b. Coupling of N7-methyltransferase and 3'-5' exoribonuclease with SARS-CoV-2 polymerase reveals mechanisms for capping and proofreading. Cell 184, 3474–3485. e11.

Ye, Z.W., Ong, C.P., Tang, K., Fan, Y., Luo, C., Zhou, R., Luo, P., Cheng, Y., Gray, V.S., Wang, P., Chu, H., Chan, J.F., To, K.K., Chen, H., Chen, Z., Yuen, K.Y., Ling, G.S., Yuan, S., Jin, D.Y., 2022. Intranasal administration of a single dose of a candidate live attenuated vaccine derived from an NSP16-deficient SARS-CoV-2 strain confers sterilizing immunity in animals. Cell. Mol. Immunol. 19, 588–601.

Zeng, C., Wu, A., Wang, Y., Xu, S., Tang, Y., Jin, X., Wang, S., Qin, L., Sun, Y., Fan, C., Snijder, E.J., Neuman, B.W., Chen, Y., Ahola, T., Guo, D., 2016. Identification and characterization of a ribose 2'-O-methyltransferase encoded by the ronivirus branch of nidovirales. J. Virol. 90, 6675–6685.

Zhou, Y., Ray, D., Zhao, Y., Dong, H., Ren, S., Li, Z., Guo, Y., Bernard, K.A., Shi, P.Y., Li, H., 2007. Structure and function of flavivirus NS5 methyltransferase. J. Virol. 81, 3891–3903.

Ziebuhr, J., 2005. The coronavirus replicase. Curr. Top. Microbiol. Immunol. 287, 57–94.

Zust, R., Cervantes-Barragan, L., Habjan, M., Maier, R., Neuman, B.W., Ziebuhr, J., Szretter, K.J., Baker, S.C., Barchet, W., Diamond, M.S., Siddell, S.G., Ludewig, B., Thiel, V., 2011. Ribose 2'-O-methylation provides a molecular signature for the distinction of self and non-self mRNA dependent on the RNA sensor Mda5. Nat. Immunol. 12, 137–143.